The Astrophysical Journal, 608:166–178, 2004 June 10

NONTHERMAL HARD X-RAY EMISSION IN GALAXY CLUSTERS OBSERVED WITH THE *BeppoSAX* PDS

J. Nevalainen,[1,2,3] T. Oosterbroek,[2] M. Bonamente,[3] and S. Colafrancesco[4]

Received 2002 July 3; accepted 2003 November 7

ABSTRACT

We study the X-ray emission in a sample of galaxy clusters using the *BeppoSAX* PDS instrument in the 20–80 keV energy band. We estimate the nonthermal hard X-ray (HXR) cluster emission by modeling the thermal contribution from the cluster gas and the nonthermal contamination from the unobscured active galactic nuclei (AGNs) in the clusters. We also evaluate the systematic uncertainties due to the background fluctuations. Assuming negligible contamination from the obscured AGNs, the resulting nonthermal component is detected at a 2 σ level in $\sim$50% of the nonsignificantly AGN-contaminated clusters: A2142, A2199, A2256, A3376, Coma, Ophiuchus, and Virgo. The data are consistent with a scenario whereby relaxed clusters have no hard X-ray component of nonthermal origin, whereas merger clusters do, with a 20–80 keV luminosity of $\sim 10^{43}$–$10^{44}\ h_{50}^{-2}$ ergs s^{-1}. The co-added spectrum of the above clusters indicates a power-law spectrum for the HXR emission with a photon index of $2.8^{+0.3}_{-0.4}$ in the 12–115 keV band, and we find indication that it has extended distribution. These indications argue against significant contamination from obscured AGNs, which have harder spectra and a centrally concentrated distribution. These results are supportive of the assumption of the merger shock acceleration of electrons in clusters, which has been proposed as a possible origin of the nonthermal hard X-ray emission models. Assuming that the cosmic microwave background photons experience inverse Compton scattering from the merger-accelerated relativistic electrons and thus produce the observed HXR, the measured hard X-ray slope corresponds to a differential momentum spectra of the relativistic electrons with a slope of $\mu = 3.8$–5.0. In presence of cluster magnetic fields this relativistic electron population produces synchrotron emission with a spectral index of 1.4–2.1, consistent with radio halo observations of merger clusters. Thus both hard X-ray and radio observations of merger clusters are consistent with the inverse Compton model. The observed slope of the HXR emission is also consistent with that predicted by the nonthermal bremsstrahlung, which thus cannot be ruled out by the fit to the current data, even though this model requires an extreme, untenable cluster energetics. Assuming a centrally concentrated distribution of HXR emission, the data require a harder slope for the HXR spectrum, which is consistent with secondary electron models, but this model yields a worse fit to the PDS data and thus seems to be disfavored over the primary electron inverse Compton model.

Subject headings: galaxies: clusters: general — X-rays: galaxies: clusters

1. INTRODUCTION

Nonthermal hard X-ray (HXR) emission has recently been observed in several clusters and groups of galaxies with the MECS and PDS instruments on board *BeppoSAX* and with GIS instrument on board *ASCA*. In the cases of Coma (Fusco-Femiano et al. 1999), A2256 (Fusco-Femiano et al. 2000), HCG 62 (Fukazawa et al. 2001), and A754 (Fusco-Femiano et al. 2003), detection of excess emission above the contribution from the hot intracluster medium (ICM) is statistically significant, while marginal evidence is provided for A3667 (Fusco-Femiano et al. 2001) and A2199 (Kaastra et al. 1999).

Most models of the HXR emission involve a population of electrons accelerated in the cluster medium. A natural source of acceleration in clusters is provided by merger shocks. In a strong cluster merger event, the electrons are accelerated to relativistic speeds (e.g., Bell 1978a, 1978b; Fujita & Sarazin 2001; Takizawa & Naito 2000). The inverse Compton scattering of cosmic microwave background photons from the relativistic electrons in clusters then can produce a nonthermal tail that exceeds the thermal bremsstrahlung emission at energies above 20 keV (e.g., Sarazin 1999; Blasi & Colafrancesco 1999). This model has been proposed as the simplest possible explanation of the HXR properties of galaxy clusters. If the acceleration is provided by a less energetic merger or turbulence (e.g., Ensslin et al. 1999), or if there is a high-energy cutoff in the electron velocity distribution, the resulting electron population is effectively transrelativistic. In this case, the dominating mechanism in producing hard X-rays has been proposed to be nonthermal bremsstrahlung (e.g., Sarazin & Kempner 2000). However, this solution faces some crucial problems mainly concerning the large energy injection required by such a mechanism and the resulting large heating expected (e.g., Petrosian 2001).

In the secondary electron population models the merger shocks and galaxy activity accelerate and inject large quantities of relativistic protons into the cluster atmosphere. Most of the relativistic protons can be confined and accumulated in the cluster medium for very long times, comparable with the cluster age $\sim H_0^{-1}$, and can then produce secondary electrons via proton-proton collisions (e.g., Colafrancesco & Blasi 1998). The energy losses are balanced by the continuous refilling of the new electrons produced in situ (i.e., continuously in time and everywhere in space). Thus the resulting HXR spectrum in the secondary models reflects the electron spectrum right after the acceleration event, while in the primary models the more

[1] Harvard-Smithsonian Center for Astrophysics, Cambridge; jukka@head-cfa.harvard.edu.
[2] ESTEC, Noordwijk, Netherlands.
[3] University of Alabama in Huntsville, Huntsville.
[4] INAF-Osservatorio Astronomico di Roma, Rome, Italy.

energetic electrons loose energy rapidly and the HXR spectrum steepens accordingly with time.

In the present work, we expand the database of cluster hard X-ray emission by studying a sample of clusters observed with the *BeppoSAX* PDS. We model the thermal and active galactic nucleus (AGN) contributions in the sample in order to obtain estimates for the nonthermal component. We propagate the modeling uncertainties, as well as the background fluctuation uncertainties, in order to obtain reliable (and somewhat conservative) estimates for the nonthermal component. We furthermore study the co-added nonthermal hard X-ray spectrum of the sample, in order to investigate the origin of this emission.

We consider uncertainties and significances at 1 σ level and use $H = 50 \times h_{50}$ km s^{-1} Mpc^{-1}, unless stated otherwise. We define HXR in this paper as 20–80 keV PDS net count rate, after removing the sky background, cluster thermal component, and AGN contamination.

2. PDS ANALYSIS

The sample consists of all publicly available clusters (as of 2001 June) observed with *BeppoSAX* whose temperatures are constrained within ~10%.

2.1. *Data Processing*

The observations were processed using SAXDAS 2.2.1. Extreme care was taken during the processing of the PDS data. We removed spikes, which are caused by charged particles hitting only one of the collimators, using the method described by F. Fiore, M. Guinazzi, & P. Grandi.[5] The effect of the spike removal was negligible compared with the statistical uncertainties.

For A1795, A2163, A2256, A3667, and Coma the observations were divided into several exposures, and A3627 has several available pointings. The data sets were processed separately, and the resulting spectra were co-added.

In order to improve the signal-to-noise ratio (S/N) we restricted the PDS analysis to the 20–80 keV band and binned the data to contain a single bin covering this band.

2.2. *Background Subtraction*

The total background in the 20–80 keV band is ~10 counts s^{-1} (Frontera et al. 1997b). Because the clusters in our sample have lower count rates than the background, we addressed carefully the uncertainties involved in the background subtraction. In the standard observing mode, the PDS system of two identical collimators is rocked back and forth after each 96 s, keeping one collimator at all times pointed at the X-ray target, to allow the simultaneous monitoring of source and background (Frontera et al. 1997a). In the standard data processing, both offset-positions (3°.5 away from the source) are used for the background subtraction. The allowed upper limit for the background modulation with the rocking collimator offset angle is only 2% (Frontera et al. 1997a). Possible variations in the cosmic-ray–induced internal background due the changing environment are addressed by the standard method of subtracting the simultaneous background spectrum obtained from regions close to the source. The hard X-ray sky background is composed mostly of discrete sources (absorbed AGNs) and is not uniform (e.g., Comastri et al. 1995). Fluctuations in the number and flux of the sources could give rise to a significant uncertainty in the background subtraction. Related to this is the effect of the presence of weak sources in only one of the offset-positions that is used for the background subtraction (the same effect as described above, except that the strength of the source is such that it is discernible in one pointing). In order to estimate the effect of random faint sources (e.g., weak AGNs) in the field of view (FOV) in the offset positions, we determined the count rates for the cluster using only one of the two (either the negative or positive direction). A clear difference between the spectra could indicate the presence of source(s) in the offset position. Note that when using only one offset position for the background the exposure time of the background is effectively halved, which results in a larger uncertainty in the source fluxes.

Initially, in order to test the robustness of the standard method in the case of no background fluctuations, we used a small sample of 12 pointings (Polaris, Lockmann hole, secondary pointings) in which no sources (other than "background") are thought to be present. From this we concluded that the mean 20–80 keV flux is very close to zero [$-(0.4 \pm 3.7)10^{-2}$ counts s^{-1}] when using the standard background subtraction, indicating that the systematic uncertainty of the standard background subtraction is negligible compared with statistical errors (Table 1). However, when using either the positive or negative offset directions only we noticed a systematic difference of ~0.06 counts s^{-1} between these two, with the positive pointings giving higher background-subtracted source count rates.

In order to study the above difference due to different offset pointings in more detail we selected a sample of 164 pointings for which the (non–spike-filtered) exposure times were larger than 20 ks (in order to have similar exposures to the cluster sample) and for which the count rate obtained with the standard processing (including spike filtering) is between -0.1 and 0.1 counts s^{-1}. These criteria were chosen in order to select either blank fields or faint sources. The mean exposure time ranges between 19.1 and 78.3 ks with a mean of 32.2 ks. The spatial distribution of the analyzed pointings is rather uniform. We find (see Fig. 1) that the mean count rate as obtained through the standard analysis is 0.027 ± 0.051 counts s^{-1}, which suggests a nonsignificant detection in the *whole* sample. The difference between the count rates obtained with either the negative or positive offset direction amounts to 0.058 counts s^{-1}, and the distributions are symmetric about the mean obtained with the standard analysis. We therefore use a correction of 0.029 counts s^{-1} (with the proper sign) whenever we use the count rates obtained using only one offset position. A possible reason for this effect could either be the effect of radiation entering the collimators from the side, screening of the instruments by the satellite, or the fact that the detector is looking at more/less radioactive parts of the satellite.

Furthermore, we quantified the effect of the background fluctuations. To do this, we used the above sample of 164 pointings to compute the differences in background-subtracted count rates between positive and negative background pointing directions. We divided them into four exposure time bins (23, 35, 44, and 60 ks) and determined the widths (σ) of the obtained distributions. The widths decrease with increasing exposure time, as expected since the widths of the distributions can be described by $\sigma^2 = \sigma^2_{\rm stat} + \sigma^2_{\rm fluc}$, where $\sigma_{\rm stat}$ is the statistical uncertainty (dependent on the total number of counts in the background or the exposure time) and $\sigma^2_{\rm fluc}$ is due to the real background variations. We then assumed that $\sigma_{\rm stat}$ is proportional to $\sqrt{t}$ (where t is the exposure time) and fitted this function, obtaining $\sigma_{\rm fluc} = 0.027$ counts s^{-1}. In the standard background subtraction the uncertainty introduced by the

[5] http://heasarc.gsfc.nasa.gov/docs/sacs/abc/sacsabc/sacsabc.html.

TABLE 1
RESULTS FOR HXR EMISSION

Name (1)	PDS Count Rate[a] (2)	CL_{det} σ (3)	Thermal[a] (4)	AGN[a] (5)	HXR[a] (6)	CL_{HXR} σ (7)	HXR_{90}[a] (8)	L_{HXR}[b] (9)	$L_{HXR_{90}}$[b] (10)
A85	11.6 ± 4.3 (−)	2.7	4.1 ± 0.8	...	$7.6^{+4.4}_{-4.4}$	1.7	14.8	$10.7^{+6.3}_{-6.3}$	21.1
A348	−1.6 ± 3.7	...	...	...	...	...	...	...	...
A496	3.7 ± 3.4	1.1	1.5 ± 0.4	...	2.3 ± 3.5	0.7	8.0	1.3 ± 2.0	4.6
A1367	2.1 ± 3.1	0.7	0.4 ± 0.2	$1.0^{+0.4}_{-0.3}$	0.7 ± 3.1	0.2	5.9	0.2 ± 0.8	1.6
A1750	1.6 ± 4.0 (−)	0.4	...	...	...	...	...	...	...
A1795	3.0 ± 2.9	1.0	$3.7^{+0.7}_{-0.6}$	0.3 ± 0.1	−1.0 ± 3.0	...	3.9	−2.0 ± 6.0	7.8
A2029	2.0 ± 4.8	0.4	8.9 ± 1.3	0.2 ± 0.1	−7.1 ± 5.0	...	1.0	−22.0 ± 15.3	3.2
A2142	25.0 ± 4.4 (+)	5.7	$11.9^{+1.6}_{-1.8}$	$3.0^{+0.8}_{-0.6}$	10.1 ± 4.8	2.1	18.0	42.0 ± 19.7	74.6
A2163	8.3 ± 3.3	2.6	6.5 ± 0.9	...	1.8 ± 3.4	0.5	7.4	38.6 ± 73.1	159.4
A2199	9.2 ± 3.4	2.7	1.6 ± 0.4	$0.6^{+0.4}_{-0.3}$	7.1 ± 3.4	2.1	12.7	3.4 ± 1.6	6.0
A2256	11.6 ± 2.9	4.0	4.1 ± 0.5	...	7.5 ± 2.9	2.5	12.3	13.6 ± 5.3	22.3
A2390	9.4 ± 4.4 (−)	2.1	...	...	...	...	...	...	...
A3266	9.5 ± 3.8	2.5	6.4 ± 1.0	$0.2^{+0.1}_{-0.1}$	2.9 ± 3.9	0.8	9.3	4.8 ± 6.4	15.4
A3376	9.5 ± 3.0	3.2	0.4 ± 0.2	$0.9^{+0.3}_{-0.2}$	8.2 ± 3.0	2.7	13.1	9.2 ± 3.4	14.7
A3562	6.8 ± 5.1 (−)	1.3	0.9 ± 0.6	...	5.8 ± 5.2	1.1	14.3	8.0 ± 7.1	19.7
A3571	−1.7 ± 4.6 (+)	...	3.0[c]	...	−4.8 ± 4.6	...	2.8	−4.1 ± 3.9	2.4
A3627	11.4 ± 3.4	3.3	6.8 ± 0.6	$6.1^{+2.4}_{-1.5}$	$-1.5^{+3.8}_{-4.2}$	...	4.7	$-0.2^{+0.6}_{-0.7}$	0.8
A3667	8.2 ± 2.6	3.2	4.4 ± 0.4	$1.7^{+0.6}_{-0.4}$	2.1 ± 2.7	0.8	6.4	3.2 ± 4.1	9.9
Coma	40.2 ± 3.4	11.8	30.9 ± 0.8	0.9 ± 0.6	8.4 ± 3.5	2.4	14.3	2.6 ± 1.1	4.4
Cygnus A	58.6 ± 3.4	17.1	...	$51.1^{+11.8}_{-9.1}$	...	...	...	...	...
Ophiuchus	75.0 ± 3.9	19.3	$66.2^{+2.0}_{-1.2}$	...	$8.8^{+4.1}_{-4.3}$	2.0	15.5	3.7 ± 1.8	6.6
Perseus	54.7 ± 3.5	15.7	37.6 ± 0.6	...	...	...	...	...	...
PKS 0745−191	3.5 ± 3.3	1.1	...	...	...	...	...	...	...
RX J0152.7−135.7	0.8 ± 3.0	0.3	...	...	...	...	...	...	...
PX J1347.5−1145	6.8 ± 4.4 (−)	1.5	...	...	...	...	...	...	...
Virgo	27.5 ± 5.5	5.0	0.3 ± 0.2	4.5 ± 0.7	22.8 ± 5.6	4.1	31.9	0.17 ± 0.04	0.24
z3146	1.4 ± 4.4	0.3	...	...	...	...	...	...	...

NOTES.—Columns are as follows. Col. (1): Name. Col. (2): The PDS count rates obtained with PDS in the 20–80 keV band using the standard background subtraction method (default) or using only positive (+) or negative (−) background pointing and correcting for the systematic effect. The errors include both statistical and systematic uncertainties at the 1 σ level. Col. (3): CL_{det} gives the confidence level of source detection. Col. (4): "Thermal" gives the thermal model prediction in the 20–80 keV band, normalized to PDS 12–20 keV data, together with 1 σ uncertainty due to PDS photon statistics in the 20– 80 keV band. Col. (5): "AGN" gives the estimated unobscured AGN contribution to the PDS 20–80 keV band. Cols. (6) HXR and (7) CL_{HXR} give the nonthermal, AGN-subtracted count rate with 1 σ errors and its confidence level. Col. (8): HXR_{90} gives the 90% confidence upper limit of the count rate of the nonthermal emission. Col. (9): L_{HXR} gives the luminosity of the AGN-subtracted nonthermal component obtained by normalizing a power law with photon index $\alpha_{ph} = 2.0$ to HXR, and its 1 σ uncertainties. Col. (10): $L_{HXR_{90}}$ gives the the 90% confidence upper limit of the HXR luminosity.

[a] 10^{-2} counts s^{-1} in the PDS 20–80 keV band.

[b] 10^{43} h_{50}^{-2} ergs s^{-1} in the 20–80 keV band.

[c] Predicted.

background fluctuations should be lower by a factor $\sqrt{2}$, i.e., 0.019 counts s^{-1}, since two background fields are used. In the following analysis we use this value as a systematic error in the background-subtracted source count rates when using the standard method and the above value 0.027 counts s^{-1} when only one background pointing direction (positive or negative) is used.

In Figure 2 we plot the difference between the count rates of the two different background pointings for all cluster exposures. The data give an average difference of 0.068 counts s^{-1}, very close to the value found in the blank fields above. Eight exposures deviate from the mean at the 90% confidence level, while random fluctuations would predict only four, and thus our sample is likely contaminated by point sources in background regions. Thus, we reject the more than 90% deviant pointings for clusters A85, A1750, A2142, A2390, A3562, A3571, and RX J1347.5−1145, and correct the resulting data values by the systematic shift ±0.029 counts s^{-1} found above using the blank fields (for A2163 only a fraction of the total exposure is affected and thus we make no correction for it). This removes most of the negative count-rate detections, with the notable exception of A3571. The signal of A3571 in the 20–80 keV band remains negative regardless of whether we use one offset pointing or two, indicating that possibly both background offsets are contaminated by AGNs. We chose to use the positive offset for background subtraction for A3571, because this gives a net count rate closest to zero and thus minimizes the oversubtraction due to AGNs. For the rest we use the standard method of using both positive and negative background pointings. We add the systematic errors due to the background fluctuation found above in quadrature to the statistical uncertainties of each cluster. The obtained count rates are listed in Table 1. Using the total 20–80 keV band emission, we achieve 3 σ detections in the direction of the following 10 clusters: A2142, A2256, A3376, A3627, A3667, Coma, Cygnus A, Ophiuchus, Perseus, and Virgo.

2.3. *Vignetting*

The vignetting of PDS is assumed not to vary with photon energy (Frontera et al. 1997a). It is modeled with a linear function of off-axis angle, reaching zero at 1°.3. When predicting the thermal contribution at 20–80 keV energies, we

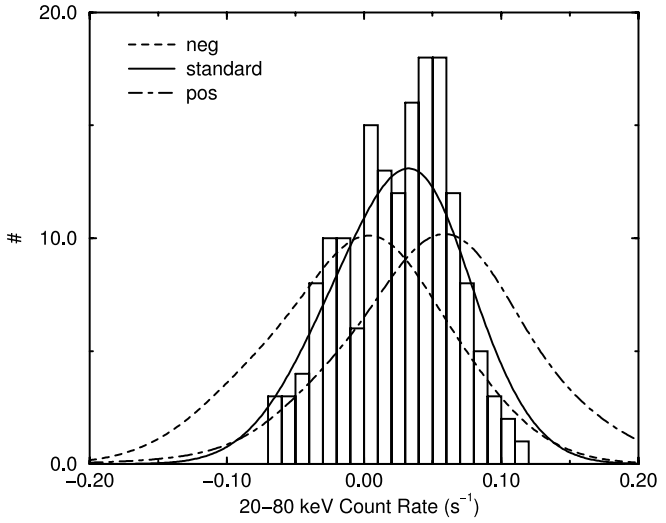

FIG. 1.—PDS count-rate distribution of the selected 164 fields in the 20–80 keV band. The histogram shows the data when the standard method of subtracting the background of both off-sets is used. The solid curve is a sum of Gaussians that represent the data points with the value of the data point as the centroid and the uncertainty as σ. The dash-dotted and dashed lines show the corresponding sum of Gaussians when only positive or negative off-sets for background subtraction are used.

use the actual PDS data (see § 3) at 12–20 keV to normalize the model, and thus the vignetting is taken care of without further work. When predicting the AGN contribution, we correct it by multiplying by the vignetting factor at the off-axis of the AGN. When deriving the nonthermal hard X-ray luminosity for a given cluster, we assume that the HXR emission is distributed like the intracluster gas, and thus we use the vignetting function and the β-model to obtain the vignetting correction to the luminosity obtained with the on-axis response. The effect of the vignetting correction to the luminosity is small, at the level of at most 20% for the closest clusters, and thus the assumption on the spatial distribution of HXR emission is not important.

3. THERMAL MODELS

We model the thermal component with XSPEC model WABS × MEKAL (see Table 2 for parameters). The *BeppoSAX* MECS study of most of these clusters reports cluster average

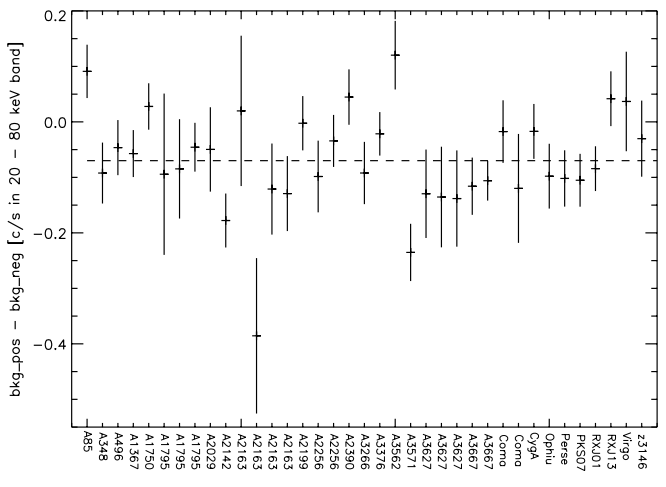

FIG. 2.—20–80 keV count-rate difference between positive and negative offset background pointings for each cluster exposure. The dashed line shows the average difference.

temperatures (de Grandi & Molendi 2002). Since in that work the central regions, affected by the presence of cooler gas (the "cooling flow scenario"), are excised from the estimates while they are included in PDS data, we preferred to use the published *ASCA* single-temperature fits (Markevitch et al. 1998) for the cooling flow clusters and *BeppoSAX* values for the non–cooling flow clusters. For the distant ($z > 0.1$) clusters only *BeppoSAX* results are available, and thus we use these regardless of the presence of any cooler gas.

MECS and *ASCA* do not cover the full FOV of PDS. Thus, because of the radially decreasing temperature profiles consistently observed with *BeppoSAX* (de Grandi & Molendi 2002) and *ASCA* (Markevitch et al. 1998), the temperatures obtained by these instruments are high compared with the global ones. For this reason we compare our adopted temperatures with results obtained for a subsample with *Ginga*, because it covers the full FOV of PDS. *Ginga* temperatures for A496, A1795, A2142, and A2199 (White et al. 1994) are systematically, and in most cases significantly, below the *ASCA* values, consistent with the radially decreasing temperature profiles. However, the thermal model predictions in the PDS 20–80 keV band using either set of values are consistent within the thermal model normalization uncertainties and thus in general the radial temperature decrease in clusters does not significantly affect the conclusions of this work.

For the nearby clusters Coma, Ophiuchus, Perseus, and Virgo, the fraction of the cluster covered by MECS and *ASCA* is small and thus the effect of decreasing temperature profiles may be significant for these. For example, the $\sim 1^\circ$ FOV *Ginga* temperatures of Coma (8.21 ± 0.16 keV; Hughes et al. 1993) and Perseus ($6.33^{+0.21}_{-0.18}$; Allen et al, 1992) are smaller than the corresponding MECS $0'$–$20'$ values (9.20 ± 0.13 keV [de Grandi & Molendi 2002] and 6.68 ± 0.08, respectively). The model prediction in the 20–80 keV band of PDS with *Ginga* parameters for Coma is significantly smaller than with *BeppoSAX* values. Thus, for the nearby Coma and Perseus Clusters we adopt the *Ginga* results. For the Virgo Cluster, *Ginga* data are not available and we use the MECS to estimate the temperature (see § 4). For Ophiuchus there are $\sim 1^\circ$ FOV *Tenma* results (11.6 keV; Matsuzawa et al. 1996), but these are at odds with the $0'$–$8'$ MECS value of 10.9 ± 0.3 keV. Using the *Tenma* value and normalizing the model to PDS 12–20 keV (see below), the model prediction is significantly above the observed emission, indicative of overestimation of the temperature. For a hot and nearby cluster such as Ophiuchus, the PDS data are of sufficiently good quality for the purpose of spectral fitting. In the Ophiuchus field there are no contaminating AGNs (see § 4) and thus we can assume that the low-energy band of PDS (12–35 keV) is dominated by the thermal emission of the whole cluster. Fitting this band with MEKAL, keeping the metal abundance fixed to 0.3 solar, we obtained a temperature of 9.1 ± 0.6 keV. The MECS and PDS values are consistent with the decreasing temperature profile (and inconsistent with *Tenma* values), and thus we adopt our PDS results for the thermal model of Ophiuchus.

In order to normalize the above models to the larger (radius of $1\overset{\circ}{.}3$) FOV of PDS, we fitted the thermal models to the 12–20 keV band PDS data with the normalization as the only free parameter. To check the robustness of the fit, we predicted the normalization using β-models to compute the increment of the model normalization between the region where the cluster model has been normalized, usually by *ROSAT* PSPC (Ebeling et at. 1996), and the PDS FOV. The fitted and predicted normalizations differ by more than 50% for the

TABLE 2
THERMAL MODELS

Name	z	N_H (10^{20} atoms cm^{-2})	I_1/I_2	r_{c1} (arcmin)	r_{c2} (arcmin)	β	$L_{78'}$[c]	T (keV)	Abundance (solar)	References (β, T, L)
A85	0.052	2.7	0.08	3.9	0.72	0.66	10.3	$6.9^{+0.4}_{-0.4}$	...	1, 2, 3
A348	0.274	3.1	Standard	Standard	Standard	Standard	3.7	$4.3^{+1.6}_{-0.8}$	...	4, 5, 5
A496	0.033	4.2	0.05	4.0	0.55	0.65	4.3	$4.7^{+0.2}_{-0.2}$	...	1, 6, 3
A1367	0.021	2.4	...	10.0	...	0.61	3.7	$3.69^{+0.10}_{-0.10}$	...	1, 7, 3
A1750	0.086	2.4	Standard	Standard	Standard	Standard	3.2	$4.46^{+0.24}_{-0.24}$	$0.30^{+0.10}_{-0.10}$	4, 7, 8
A1795	0.062	1.0*	0.07	3.5	0.82	0.79	12.1	$7.8^{+1.0}_{-1.0}$	...	1, 2, 3
A2029	0.077	3.2*	0.05	2.8	0.68	0.71	17.2	$9.1^{+1.0}_{-1.0}$	...	1, 2, 3
A2142	0.089	4.1*	0.07	4.8	1.2	0.79	22.5	$9.7^{+1.5}_{-1.1}$	...	1, 2, 3
A2163	0.203	11.9	...	1.6	...	0.73	43.3	11.5	...	9, 10, 3
A2199	0.030	0.86*	0.18	3.2	0.81	0.66	4.4	$4.8^{+0.2}_{-0.2}$	...	1, 6, 3
A2256	0.058	4.5*	...	5.3	...	0.83	8.2	$6.97^{+0.12}_{-0.12}$	$0.26^{+0.02}_{-0.02}$	1, 7, 3
A2390	0.228	7.0	...	0.47	...	0.60	26.3	$9.8^{+0.8}_{-0.7}$	$0.3^{+0.1}_{-0.1}$	11, 12, 3
A3266	0.055	1.6*	...	5.7	...	0.74	8.1	$8.97^{+0.30}_{-0.30}$	$0.22^{+0.03}_{-0.03}$	1, 7, 3
A3376	0.046	4.4*	Standard	Standard	Standard	Standard	3.0	$3.99^{+0.13}_{-0.13}$	$0.23^{+0.04}_{-0.04}$	4, 7, 3
A3562	0.050	3.8	...	1.2	...	0.47	7.1	$5.1^{+0.3}_{-0.3}$	$0.39^{+0.08}_{-0.08}$	1, 13, 3
A3571	0.040	4.1*	...	2.6	...	0.61	9.7	$6.9^{+0.2}_{-0.2}$	...	1, 2, 3
A3627	0.016	21.9	...	10.0	...	0.56	3.8	$6.28^{+0.18}_{-0.18}$	$0.27^{+0.02}_{-0.02}$	14, 7, 3
A3667	0.053	4.8	...	3.1	...	0.54	14.4	$7.0^{+0.6}_{-0.6}$	...	1, 2, 3
Coma	0.023	0.9	...	10.1	...	0.71	8.8	$8.21^{+0.16}_{-0.16}$	$0.21^{0.03}_{-0.03}$	1, 15, 3
Cygnus A	0.057	36.1	...	0.17	...	0.47	15.5	$6.9^{+1.5}_{-1.3}$	$0.67^{+0.12}_{-0.10}$	1, 2, 2
Ophiuchus	0.028	20.3*	0.65	5.8	1.7	0.71	13.5	$9.1^{+0.6}_{-0.5}$	$0.49^{+0.08}_{-0.08}$	1, 8, 8
Perseus	0.018	14.8	0.02	13.1	2.0	0.75	9.6[e]	$6.33^{+0.21}_{-0.18}$	$0.41^{+0.02}_{-0.02}$	1, 16, 8
PKS 0745−191	0.103	42.4	Standard	Standard	Standard	Standard	...	$8.5^{+0.6}_{-0.6}$	$0.38^{+0.03}_{-0.03}$	4, 17, ...
RX J0152.7−135.7	0.831	1.6	Standard	Standard	Standard	Standard	11.6	$6.5^{+2.9}_{-2.0}$	$0.5^{+0.5}_{-0.4}$	4, 18, 18
RX J1347.5−1145	0.451	4.8	...	0.14	...	0.56	58.4	$14.3^{+1.8}_{-1.5}$	$0.5^{+0.2}_{-0.2}$	19, 12, 12
Virgo	0.0036	2.5	...	2.2	...	0.45	0.7[e]	$2.35^{+0.06}_{-0.06}$	$0.49^{+0.06}_{-0.06}$	20, 8, 8
z3146	0.291	3.0	Standard	Standard	Standard	Standard	28.3	$7.3^{+0.9}_{-0.8}$	$0.3^{+0.1}_{-0.1}$	4, 12, 12

[a] The N_H values are based on Dickey & Lockman (1990), except for the ones marked with asterisks, which are taken from fine-beam H II survey (thin filter) of Murphy et al. (2004, in preparation).
[b] The β-model parameter reference (4) corresponds to the STANDARD model of $\beta = \frac{2}{3}$ and $r_{c1} = 0.2\ h_{50}^{-1}$ Mpc, due to lack of proper reference.
[c] The unabsorbed luminosities $L_{78'}(10^{44}\ h_{50}^{-2}\ \mathrm{ergs\ s^{-1}})$ in the 0.1–2.4 keV band are obtained by using the β-models to extrapolate the luminosities taken from the references papers.
[d] The abundances, where marked, are taken from the temperature references; otherwise 0.3 solar is assumed.
[e] Power-law component removed.
REFERENCES.—(1) Mohr et al. 1999; (2) Markevitch et al. 1998; (3) Ebeling et al. 1996; (4) STANDARD; (5) Colafrancesco & Mele 2001; (6) Markevitch et al. 1999a; (7) de Grandi & Molendi 2002; (8) this work, (9) Vikhlinin et al. 1999; (10) Markevitch et al. 1996; (11) Böhringer et al. 1998; (12) Ettori et al. 2001; (13) Ettori et al. 2000; (14) Böhringer et al. 1996; (15) Hughes et al. 1993; (16) Allen et al. 1992; (17) de Grandi & Molendi 1999a; (18) Della Ceca et al. 2000; (19) Schindler et al. 1997; (20) Böhringer et al. 1994.

faint clusters (A348, A1750, A2390, PKS 0745−191, RX J0152.7−135.7, RX J1347.5−1145, and Zw 3146), probably because of large statistical uncertainties in the 12–20 keV data. Thus we reject these clusters from further analysis. For the rest these two methods give values that differ by less than 40%, which can be explained by the uncertainties involved in the radial extrapolation and the cross-calibration uncertainty between PDS and PSPC. We prefer to use the fitted values, because they should be devoid of these uncertainties.

In Virgo, Perseus, and Cygnus A the 2–10 keV band data are strongly contaminated by AGNs. Thus, when normalizing the thermal model, the AGN contribution must be taken into account. We will describe this in detail in § 4.

As a further check of the bright AGNs in background fields, we compared the obtained thermal model normalizations in the 12–15 and the 15–20 keV energy bands. The appearance of an AGN in only one background field would result in different normalizations using either positive or negative pointing for background subtraction. Also, if the spectrum of an AGN is not identical to that of the cluster in the 10–20 keV band, its appearance would result in different normalization using either the 12–15 or the 15–20 keV band. We found that in the 15–20 keV band in all clusters, except A3571, both offsets give consistent values for the normalization of the thermal model. In the 12–15 keV band, clusters A3571 and A2142 give inconsistent values between the two offsets. Therefore, for A2142 we use only the 15–20 keV band for the normalization, and for A3571 we use the predicted normalization.

The obtained model predictions are listed in Table 1. The reported uncertainties of the thermal models include only the statistical uncertainty due to the PDS data in the 12–20 keV band. In most cases this is negligible compared with the PDS 20–80 keV count-rate uncertainties. We previously discovered that for a subsample of clusters, possible hot ICM temperature variations result in negligible variation of the thermal model prediction in the 20–80 keV band. Assuming that this holds for the whole sample, propagating the model normalization uncertainty only is adequate to estimate the uncertainties in the thermal model.

4. AGNs

In the large field of view of PDS, the 20–80 keV band emission may be contaminated by AGNs and QSOs randomly projected in the line of sight or AGNs belonging to the cluster under study. In optical surveys it was found that most of the nearby AGNs (∼80%) are optically faint Seyfert 2 galaxies

(e.g., Maiolino & Rieke 1995). In the unified AGN scheme the optically bright and identifiable AGNs or Seyfert 1 galaxies are the ones observed face-on with no obscuration by the torus. Most of the lines of sight to the AGN nucleus are intersected by the absorbing torus, and thus most of the AGNs are obscured ($N_{\rm H} = 10^{22}$–10^{25} atoms cm^{-2}; Risaliti et al. 1999) and optically faint Seyfert 2 galaxy. Recent deep X-ray observations of blank fields (e.g., Hasinger et al. 2001) have consistently discovered a population of absorbed point sources that outnumbers the Seyfert 1 galaxies by a factor of $\sim$4. In addition, a population synthesis modeling of cosmic X-ray background (Gilli et al., 1999) indicates that 80% of the AGNs need to be obscured to produce the CXB spectrum, which is harder than the spectrum of unobscured AGNs.

The local background has been subtracted from the PDS data, and thus the effect of random AGNs and QSOs in a given line of sight should have been removed from our results. However, there is evidence that the AGN density *inside* clusters is enhanced by a factor of 2 compared with noncluster fields (Molnar et al. 2002; Cappi et al., 2001; Sun & Murray 2002), perhaps because of galaxy-galaxy interactions. Their contribution is not removed by the standard background subtraction, and thus we need to estimate the number of the excess AGNs in clusters (compared with blank fields). The unobscured AGNs are optically identifiable and soft X-ray–bright. Thus, it is feasible to find them from optical catalogs and soft X-ray images and to estimate their contribution to HXR emission, as we describe in § 4.1. However, the obscured AGNs are a difficult problem for the HXR studies, because the high obscuration by the torus may hide them in the less than 10 keV band and make the optical detection difficult. At 20–80 keV energies, $N_{\rm H}$ has no effect and the obscured AGNs may give a significant contribution in this band. We estimate this contribution in § 4.2.

4.1. *Unobscured AGNs*

A combined *ASCA* 2–10 keV spectrum of 13 unobscured *ROSAT* International X-Ray Optical Survey (RIXOS) AGNs (Page, 1998) has a photon index of 1.8 ± 0.1. Perola et al. (2002) studied nine bright Seyfert 1 galaxies in the 0.1–200 keV band using *BeppoSAX* LECS+MECS+PDS data. Their results indicate that in the 20–80 keV band the photon index is 1.8 on average, with a standard deviation of 0.1, while all best-fit values fall within the range 1.8 ± 0.2. These two works indicate that a slope of 1.8 is a good representation of unobscured AGN spectra and that the extrapolation of the 2–10 keV spectrum up to 80 keV is robust. In our work, when the spectral information is not available, we use a power-law model with a photon index of 1.8 ± 0.2 (at a 90% confidence level) as a reference model to estimate the Seyfert 1 contribution in the PDS 20–80 keV band data.

The variable flux level of Seyfert 1 galaxies must be taken into account. A study of 113 Seyfert 1 galaxies observed in the *ROSAT* All Sky Survey and in pointed PSPC and HRI observations (Grupe et al. 2001) shows that while a few percent of the objects in the sample are transients whose soft band flux varies by a factor of 100 in timescales of years, $\sim$90% of the AGNs vary by less than a factor of 2–3. The hardness ratio analysis is consistent with no spectral variation. A study of nine Seyfert 1 light curves in the 2–10 keV energy band with *RXTE* (Markowitz & Edelson 2001) yields results consistent with variability by less than a factor of 2. Furthermore, they exhibit stronger variability in the 2–4 keV band than in the 7–10 keV band, consistent with the *ROSAT* study. If this trend continues toward higher energies, variability by more than a factor of 2 should not be common. Thus in our analysis, when simultaneous normalization level information is not available, we include $\pm$50% uncertainty (a factor of 3 variation between lower and upper limit at 90% confidence level) for the AGN contribution to PDS data.

We searched the SIMBAD database for non-Seyfert 2 AGNs within $1\overset{\circ}{.}3$ of the FOV center (we perform a separate treatment for Seyfert 2 AGNs in § 4.2). We limited the search to AGNs whose redshifts indicate that they belong to the cluster under study. For each cluster, we studied the three best-known objects (see Table 3). We also cross-examined the MECS and PSPC images of the clusters in our sample for additional bright point sources. Because of a smaller PSF, we used PSPC instead of MECS to identify point sources and then examined the corresponding MECS image for excess emission in that sky position. We also examined MECS images for additional variable hard-band sources, which were not visible in PSPC. We assume in the following conservatively that the point sources identified here constitute the excess AGN population inside clusters, compared with the blank field population, which has not been subtracted from the PDS signal.

The estimation of the AGN contribution to PDS data is difficult since there is no spatially resolved hard X-ray spectroscopic information for our cluster sample. Thus, where possible, we use the MECS data to obtain the 2–10 keV AGN spectrum and extrapolate it to PDS energies. We subtract the local background obtained next to the AGN to ensure similar cluster contributions in both source and background data. We include the vignetting effect by using ancillary files appropriate for a given off-axis angle as provided by the *BeppoSAX* team. This method has the virtue of reducing the uncertainties of the time variability of the AGNs. However, because of the wide PSF of MECS, this approach is not accurate for the faintest off-axis sources. For those, as well as for the sources outside the MECS FOV, we use PSPC 0.4–2.0 keV count rates to normalize the reference model, considering the spectral and flux variability as described above. The details of the AGN modeling in individual cluster fields are given in the Appendix.

4.2. *Obscured AGNs*

For nearby ($z < 0.1$) Seyfert 2 galaxies to significantly affect our results, they need to produce a luminosity of $\sim L_{20-80} = 10^{43}$–10^{44} ergs s^{-1} in each PDS pointing (see § 5.1). A *Chandra* study of the A2104 cluster (Martini et al. 2002) revealed five optically unidentified point sources (Seyfert galaxies) whose total luminosity reaches 10^{43} ergs s^{-1} in the 20–80 keV band when using a power law with photon index of 2 to extrapolate from the 2–10 keV band. This indicates that Seyfert 2 galaxies can in principle affect our results.

In the unified scheme of AGNs and in the X-ray–background synthesis models it is assumed that the intrinsic luminosity distribution of the obscured and unobscured objects is the same. Assuming further that the relative Seyfert1 to Seyfert 2 number densities are similar in the field and in the cluster environments, we can estimate the 20–80 keV emission of the obscured AGNs inside a given cluster by multiplying the corresponding Seyfert contribution estimated above by a factor of 4. The number of galaxies in typical rich clusters is of the order of 100, and thus the assumed number of AGNs is only a few per cluster, which introduces problems of small number statistics. In some clusters there are no cataloged Seyfert 1 galaxies and thus no predicted Seyfert 2 signal. On the other hand, in clusters A1367, A1795, A2029, A2142, A3627, A3667, and Cygnus A the Seyfert

TABLE 3
OBSERVATION LOG AND AGN INFORMATION

Cluster	Exposure Start	Exposure End	PDS Exposure Time (ks)	PSPC Seq_ID	R.A. (J2000.0)	Decl. (J2000.0)	AGN	Type
A85.....	1998 Jul 18	1998 Jul 20	42	RP800250N00	00 41 30	−09 23 00	None	
A496.....	1998 Mar 5	1998 Mar 7	42	RP800024N00	04 33 38	−13 15 43	None	
A1367.....	1999 Dec 21	1999 Dec 23	46	RP800153N00	11 44 29	19 50 02		
					11 45 05	19 36 22	NGC 3862	AGN
					11 46 12	20 23 28	NGC 3884	LINER
A1795.....	1996 Dec 29	1996 Dec 29	5	RP800105N00	13 48 50	26 35 30		
	1997 Aug 11	1997 Aug 12	13		13 48 52	26 35 34	PKS 1346+26	LINER
	2000 Jan 26	2000 Jan 28	42		13 48 35	26 31 08	1E1346+26.7	Seyfert 1
					13 43 57	27 12 41	RX J1343.9+2712	AGN
A2029.....	1998 Feb 4	1998 Feb 5	18	RP800249N00	15 10 56	05 44 38		
					15 11 41	05 18 09	JVAS B1509+054	Seyfert 1
					15 11 34	05 45 46	QSO J1511+057	AGN
A2142.....	1997 Aug 26	1997 Aug 28	44	RP800415N00	15 58 20	27 14 00		
					16 02 09	26 19 46	IC 1166	Seyfert 1
					15 59 23	27 03 37	QSO B1557+272	Seyfert 1
					15 58 29	27 17 08	1E 1556+27.4	Seyfert 1
A2163.....	1998 Feb 6	1998 Feb 7	5	RP800188N00	16 15 18	−06 07 11	None	
	1998 Feb 21	1998 Feb 22	5		16 15 18	−06 07 11	None	
	1998 Feb 23	1998 Feb 24	15		16 15 18	−06 07 11	None	
	1998 Mar 3	1998 Mar 4	22		16 15 18	−06 07 11	None	
A2199.....	1997 Mar 21	1997 Mar 23	42	RP800644N00	16 28 38	39 33 05	None	
A2256.....	1998 Feb 11	1998 Feb 12	24	RP100110N00	17 03 58	78 38 31	None	
	1999 Feb 25	1999 Feb 26	40		17 03 58	78 38 31	None	
A3266.....	1998 Mar 24	1998 Mar 26	32	RP800552N00	04 31 21	−61 26 40		
					04 38 29	−61 47 59	J043829.3−614759	Seyfert 1
					04 33 34	−60 58 30	C3266−12	AGN
					04 34 40	−60 54 06	E3266−3	AGN
A3376.....	1999 Oct 17	1999 Oct 19	54	RP800154N00	06 01 37	−39 59 25		
					05 58 50	−40 38 48	J055850.3−403848	Seyfert 1
A3562.....	1999 Jan 31	1999 Feb 1	23	RP800237N00	13 33 38	−31 40 12		
					13 37 58	−31 44 12	1E 1335.1−3128	Seyfert 1
A3571.....	2000 Feb 4	2000 Feb 6	31	RP800287N00	13 47 28	−32 51 56	None	
A3627.....	1997 Mar 1	1997 Mar 2	16	RP800382A01	16 14 22	−60 52 20	None	
A3627.....	1997 Feb 24	1997 Feb 24	13		16 16 29	−61 03 16	None	
A3627.....	1997 Mar 6	1997 Mar 6	14		16 15 52	−60 37 17	None	
A3667.....	1998 May 13	1998 May 14	36	RP800234N00	20 11 30	−56 40 00		
					20 11 59	−57 05 07	FRL 339	Seyfert 1
	1999 Oct 29	1999 Nov 1	64	RP800234N00	20 11 30	−56 40 00		
					20 11 59	−57 05 07	FRL 339	Seyfert 1
Coma	1997 Dec 28	1997 Dec 30	31	RP800005N00	12 59 35	27 56 42		
	1998 Jan 19	1998 Jan 20	11		13 00 22	28 24 03	X-Comae	Seyfert 1
					12 57 11	27 24 18	J125710.6+272418	Seyfert 1
					13 01 20	28 39 57	1E 1258+28.9	AGN
Cygnus A	1999 Oct 27	1999 Oct 28	34	RP800622N00	19 59 28	40 44 02		
					19 59 28	40 44 02	QSO B1957+405	Seyfert 1
Ophiuchus	1999 Aug 22	1999 Aug 23	26	RP800279N00	17 12 26	−23 22 33	None	
Perseus	1996 Sep 19	1996 Sep 21	38	RP800186N00	03 19 50	41 32 24		
					03 19 48	41 30 42	NGC 1275	Seyfert 1
Virgo.....	1996 Jul 14	1996 Jul 15	12	RP800187N00	12 30 50	12 25 19		
					12 30 49	12 23 28	M87	S3 or LIN

NOTES.—Units of right ascension are hours, minutes, and seconds, and units of declination are degrees, arcminutes, and arcseconds. For each cluster the times of the start and the end of each exposure are given, together with the exposure times and PDS pointing coordinates. A3627 has offset pointings, and they are listed separately. Also listed are the PSPC pointings studied in this work. The names and coordinates of the three most referenced AGNs (excluding Seyfert 2 galaxies) within 1°.3 radius from the PDS pointing centers, found from SIMBAD database, are given.

1–based estimate for the nonthermal contribution is higher than the observed nonthermal signal. Thus, we cannot form a robust Seyfert 2 contamination estimate for each cluster but rather have to resort to a sample average Seyfert 1–based estimate for the Seyfert contribution. The estimate is clearly dominated by Cygnus A and Perseus; excluding these sources, the average Seyfert 2 20–80 keV band luminosity of 4×10^{43} ergs s^{-1} is similar to the average nonthermal luminosity (6×10^{43} ergs s^{-1}) observed in the sample (see Fig. 4). Thus, if the assumptions involved in the estimation are correct, Seyfert 2 galaxies may potentially be a significant source of contamination in the 20–80 keV band.

The assumption of the similarity of field and cluster point source populations can be addressed by studying the *Chandra*

analysis of point sources in clusters. These observations reach a flux level of 10^{-15} ergs s^{-1} cm^{-2} in the 2–10 keV band (Martini et al. 2002; Sun & Murray 2002; Molnar et al. 2002). Following the observation that a substantial fraction ($\sim$50%) of Seyfert 2 galaxies are Compton-thick (Risaliti et al.), we estimate that the sample average nonthermal luminosity yields absorbed 2–10 kev fluxes of 10^{-17}–10^{-13} ergs s^{-1} cm^{-2}, when assuming a power law with $\alpha_{ph} = 2.0$ with $N_H = 10^{24}$–10^{25} cm^{-2}. Thus, *Chandra* is sensitive enough to probe a significant fraction of the predicted obscured AGNs in clusters. However, in several clusters observed with *Chandra* (e.g., Molnar et al. 2002), no such sources were found. Also, the above works indicate that the faint point sources in different clusters are of a different nature and thus do not support the above assumption of substantial fieldlike Seyfert 2 population in all clusters. Consequently, the sample average Seyfert 2 contamination level can only be taken as qualitative. In this work we use the quantitative predictions for the flux of unobscured AGNs, and discuss the possible effects of obscured AGNs in the conclusions.

5. RESULTS

5.1. *Detections*

In order to obtain the count rates of the nonthermal emission in the 20–80 keV band (HXR) we subtracted the estimated thermal emission and the unobscured AGN contribution from the PDS data and propagated the uncertainties arising from background fluctuations, PDS data statistics, and modeling of the thermal and AGN contributions (see Fig. 3 and Table 1). HXR fluxes vary between 0 and 0.1 counts s^{-1} in the 20–80 keV PDS band. The statistical uncertainties are similar for different clusters, because the PDS signal is dominated by the background and the exposure times are similar within the sample. The systematic uncertainties due to background fluctuations are comparable to the statistical ones and common for all clusters. Thus the uncertainties of the background-subtracted PDS count rates are similar in different clusters. The relative total uncertainties are quite large, ranging from 10% to several 100%. The largest errors correspond to those clusters with significant Seyfert 1 contaminations.

In the sample there are 15 clusters whose 20–80 keV band signal is not significantly contaminated by Seyfert 1 galaxies (e.g., less than 15% of the total signal, thus smaller than the statistical errors): A85, A496, A1795, A2029, A2142, A2163, A2199, A2256, A3266, A3376, A3562, A3571, Coma, Ophiuchus, and Virgo. In $\sim$50% of these, the nonthermal component is detected at 2 σ level (A2142, A2199, A2256, A3376, Coma, Ophiuchus, and Virgo). The 4 σ detection of the Virgo Cluster constitutes a separate case. Virgo is the nearest cluster, which renders its data of high S/N, and it features the coolest ICM ($\sim$2 keV), thus giving the least thermal contribution in the PDS band. Furthermore, the HXR luminosity of Virgo is 1 order of magnitude smaller than the other 2 σ detected clusters, and therefore its hard excess is more easily produced by unseen AGNs. We confirm the previously published HXR detections of Coma (Fusco-Femiano et al. 1999) and A2256 (Fusco-Femiano et al. 2000), albeit at lower confidence level because of the level of systematic uncertainties of our work. The HXR detection of A2199 would be higher than 2.1 σ if we assumed that the steep PSPC spectrum of the AGN in the field of A2199 was to be extrapolated to PDS energies, as in Kaastra et al. (1999). Again, because of our AGN modeling, our detection of A3667 is of lesser significance than that of Fusco-Femiano et al. (2001).

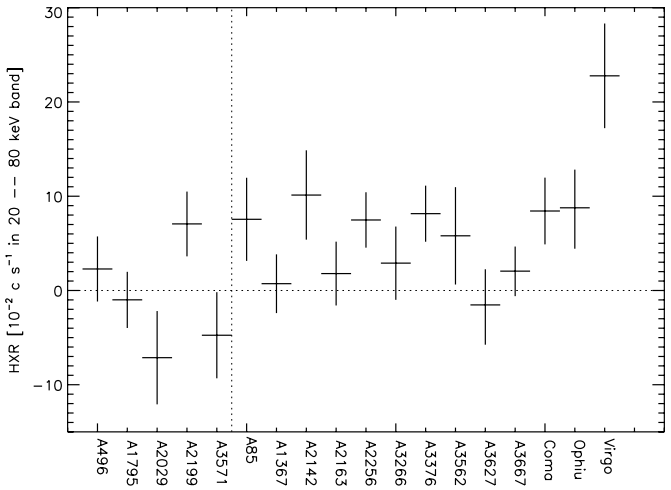

FIG. 3.—Nonthermal signal and 1 σ uncertainties in the PDS 20–80 keV band after subtraction of the contributions from the background, thermal gas, and AGNs in the field and after propagating uncertainties due to these subtractions. The dotted vertical line separates the relaxed clusters (*left*) from the rest (*right*).

All the clusters detected at 2 σ level, except A2199, exhibit some degree of merger signatures, i.e., deviations from the azimuthally symmetric brightness and temperature distributions, reported as follows: A2142 and A3376 (Markevitch et al. 1998), A2256 (Molendi, de Grandi, & Fusco-Femiano 2000), Coma (Arnaud et al. 2001), Ophiuchus (Watanabe et al. 2001), and Virgo (Shibata et al. 2001). The well-established relaxed clusters A1795, A3571 (Markevitch et al. 1998), A496 (Markevitch et al., 1999b), and A2029 (Sarazin et al. 1998) exhibit less significant detections. Thus, we divide our sample into two groups: relaxed clusters (A496, A1795, A2029, A2199, and A3571) and merger clusters (A85, A1367, A2142, A2163, A2256, A3266, A3376, A3562, A3627, A3667, Coma, and Ophiuchus), excluding Virgo, Cygnus A, and Perseus, as

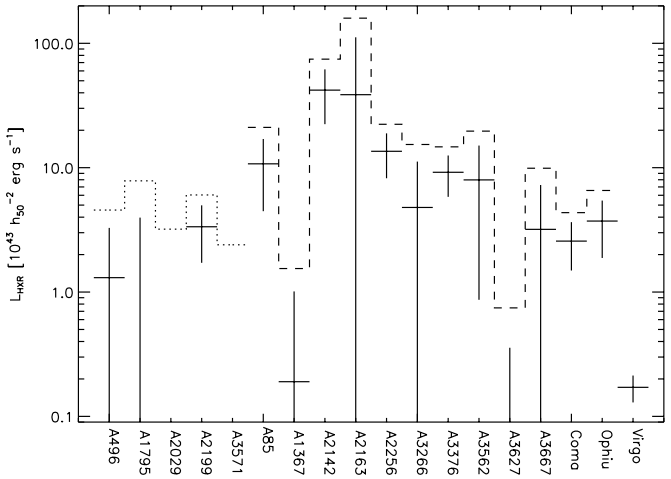

FIG. 4.—Luminositites of the nonthermal emission in the PDS 20–80 keV band at 1 σ confidence level, obtained by using a power-law model with a photon index of 2.0. The dotted and dashed lines show the allowed 90% upper limit for HXR luminosity in the relaxed and merger clusters. Note that the A3571 and A2029 values are negative at above the 1 σ level and are thus excluded from the logarithmic plot.

explained above. Assuming that the clusters in both groups lie at the group average redshift and that the intrinsic emission models are identical inside a group, we formed a weighted mean of the HXR emission and its uncertainty for both groups. This yields 0.5×10^{-2} and 4.8×10^{-2} counts s^{-1} in the PDS 20–80 keV band for the relaxed and merger groups, respectively, i.e., the count rate of the merger group is 10 times as high as that of the relaxed group. The average redshift of the relaxed group is lower (0.048) than that of the merger group (0.058), indicating that the higher count rate of the merger group is not due to a distance effect, but rather that there are intrinsic differences between the two groups. Because of the large systematic uncertainties due to background fluctuations (1.9–2.7 10^{-2} counts s^{-1}), the detection significance of the merger group remains at 2.5 σ, while the relaxed group count rate is consistent with zero.

To address the intrinsic emission we assumed that it may be modeled with a power-law model with a photon index of 2.0 and that only the normalization varies between clusters. We normalized this model to the HXR values for each cluster to obtain its luminosity $L_{\rm HXR}$ in the 20–80 keV band at the cluster's redshift. Luminosities vary from 0 to 10^{44} h_{50}^{-2} ergs s^{-1}, most values being in the range (10^{43}–10^{44}) h_{50}^{-2} ergs s^{-1} (Fig. 4 and Table 1). Using the above model and the average redshift, we converted the average count rate of the merger group into luminosity, obtaining 8×10^{43} h_{50}^{-2} ergs s^{-1}, respectively. Thus, the data are consistent with a general scenario whereby the relaxed clusters have no HXR component, while merger clusters do, with a 20–80 keV luminosity of $\sim 10^{43}$–10^{44} h_{50}^{-2} ergs s^{-1}.

6. COMBINED SPECTRUM

Individual cluster signals are of insufficient S/N for the purpose of constraining the spectral models. Thus, in order to obtain information of the average nonthermal cluster spectrum, we formed an average cluster spectrum by co-adding bin-by-bin the PDS counts of each cluster whose 20–80 keV band signal is contaminated by less than 10% by Seyfert 1 galaxies (see § 5.1), i.e., A85, A496, A1795, A2029, A2142, A2163, A2199, A2256, A3266, A3376, A3562, A3571, Coma, and Ophiuchus. The co-added exposure time is 560 ks. To avoid artificial overestimation of the uncertainties, we did not propagate the uncertainties of the individual spectra but rather used the combined spectrum to determine the Poissonian uncertainties. The level of systematic uncertainty due to background fluctuations in the 20–80 keV band is ~15% of the background-subtracted PDS signal. Since we have no information on the energy dependence of this quantity, we assumed it to be a constant 15% in the 12–115 keV band. Combining this with the uncertainty of AGN contamination, we arrive at 20% systematic uncertainty, which we use in the following analysis.

In an attempt to account for the total thermal contribution, we first fitted the 12–20 keV band data with a MEKAL model keeping metal abundance at 0.3 solar and the redshift at the median of 0.06. In this band, the typical $N_{\rm H}$ of 10^{20} cm^{-2} has no effect, and thus we exclude the absorption from the model. The best-fit temperature is consistent with the median of 7.8 keV of the sample, implying that the nonthermal emission does not dominate in the 12–20 keV band. The nonthermal excess on top of the thermal model is clearly evident: at 100 keV, the thermal model underpredicts the signal by 4 orders of magnitude (see Fig. 5 for the thermal contribution in the final best-fit model). Fitting the 12–115 keV band data with only a MEKAL model, we obtain a statistically unacceptable fit with unrealistically high temperature of 26 keV. This further confirms the existence of an additional hard X-ray component.

We introduced a power-law component to the 12–115 keV band fit, allowing the photon index and the normalization to vary, together with the MEKAL temperature and normalization. The best fit is formally acceptable, with χ^2/dof of 10.9/11, yielding a photon index of $2.8^{+0.3}_{-0.4}$ (Fig. 5). The typical AGN photon index of 1.8 is ruled out at the 98% confidence level, which argues against significant Seyfert 2 contamination in the hard X-ray signal.

However, the nonthermal emission in this model in the 12–20 keV band is high, ~50% of the total. In order to study the relative contribution of the thermal and nonthermal components, we examined the central 8′ MECS data of the largest contributors to the thermal emission in the sample, i.e., Coma and Ophiuchus, by fitting the MECS 2–10 keV data with a MEKAL plus a power law with $\alpha_{\rm ph}$ fixed to 2.8. The allowed 1 σ upper level for the nonthermal contribution, extrapolated to the 12–20 keV band, is below 1%. Thus, the above best-fit model requires that the nonthermal emission is extended and negligible in the central 8′. To confirm that this is the case, one needs to perform spatially resolved hard X-ray spectroscopic analysis on the cluster sample, which is currently not possible.

Alternately, if we assume that most of the HXR emission originates from cluster centers, the MECS data require a harder spectrum for it: fixing $\alpha_{\rm ph}$ to smaller values and keeping $N_{\rm H}$ at Galactic values, the MEKAL+power law fit to 2–10 keV MECS data of Coma and Ophiuchus allow bigger contribution from the nonthermal model in the 12–20 keV band. Also, forcing the nonthermal component in the PDS 12–115 keV fit to be harder decreases the nonthermal contribution in the 12–20 keV PDS band, and with $\alpha_{\rm ph} \leq 1.5$ the nonthermal flux at 12–20 keV in the best-fit PDS model is below 10% of the thermal, consistent with the MECS data of Coma and Ophiuchus. On the other hand, the decreasing nonthermal contribution in the 12–20 keV band requires higher temperatures for the best-fit PDS model, and at $\alpha_{\rm ph} \leq 1.3$ it exceeds the highest temperature of the cluster sample. Thus, assuming that the nonthermal emission comes mainly from the cluster centers, its photon index is limited within 1.3–1.5. However,

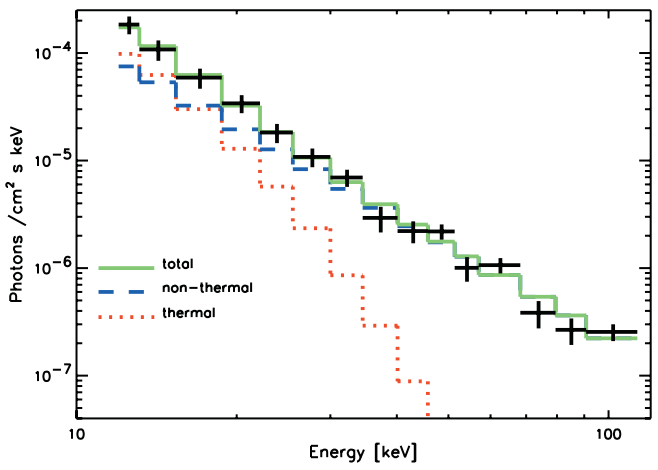

FIG. 5.—Combined spectrum of all the clusters not significantly affected by AGNs. The lines show the unfolded model components, while the crosses show the data and 1 σ errors (including 20% systematics). The solid line shows the total model. The dotted line shows the thermal contribution. The dashed line shows the best-fit power law of $\alpha_{\rm ph} = 2.8$.

such hard slopes yield poor fits to the PDS data. Keeping $\alpha_{\rm ph} \equiv 1.3$ the model has $\chi^2/{\rm dof} = 20.9/12$ and systematically exceeds the data by 20%–40% above 70 keV energies. Note that assuming an obscured AGN model with $\alpha_{\rm ph} = 1.8$ and $N_{\rm H} = 10^{25}$ cm^{-2} would yield consistence between MECS and PDS, since the high absorption in the 2–10 keV band would hide the nonthermal contribution from the MECS data but would allow it to dominate in PDS band. However, this forced fit is also significantly worse ($\chi^2/{\rm dof} = 17.2/12$) than that of the free $\alpha_{\rm ph}$ fit. Thus the data indicate that the steeper slope (2.4–3.1), and thus the extended distribution of the nonthermal emission are more likely. The Seyfert 2 galaxies inside clusters are concentrated in the central high galaxy density regions and thus the indication for extended nature of the nonthermal emission also argues against the Seyfert 2 origin of the PDS signal.

7. MODELS AND DISCUSSION

Most models for the HXR emission require acceleration of cluster electrons to suprathermal and/or relativistic velocities. Large-scale acceleration is naturally provided by merger shocks, and our findings (higher HXR detection significance of the merger clusters compared with relaxed clusters; see § 5) are consistent with this basic assumption. A strong merger accelerates electrons to relativistic velocities, and consequently the cosmic microwave background photons may experience inverse Compton scattering (IC/CMB) from these electrons, thus producing hard X-ray emission. Within the framework of the merger acceleration, the observed photon index (2.4–3.1) of the combined PDS spectrum in this work implies a power-law form for the differential momentum spectra of the relativistic ($\sim$GeV) electrons with a slope of $\mu = 3.8$–5.2. Right after the first acceleration event the primary electron distribution is predicted to be harder ($\sim$2–2.5; see Miniati et al. 2001), but the electrons loose energy rapidly and their spectrum in the GeV range steepens into consistence with that derived from the observed PDS spectrum.

The IC/CMB model requires a confinement of the relativistic electrons in clusters, which can be achieved by the cluster magnetic fields. In the presence of magnetic fields, the relativistic electrons produce synchrotron emission at radio wavelengths. Thus, the model naturally predicts a connection between the nonthermal hard X-rays and radio emission. We have indicated above a connection between the nonthermal hard X-ray emission and cluster mergers, which in turn predicts a connection between cluster mergers and radio emission. Indeed, clusters with a large-scale (>1 Mpc) radio halo possess merger signatures such as substructure in the X-ray brightness and temperature distribution and absence of cooling flows (see Feretti 2003 and references therein). Also, the diffuse radio emission is more common in clusters with higher X-ray luminosities (Giovannini et al 1999), perhaps because of energy input by recent mergers, as in hydrodynamic simulations (Sarazin et al. 2002). Thus, the observed connections of cluster mergers with radio emission and with nonthermal hard X-rays support the IC/CMB scenario whereby mergers provide higher temperatures and luminosities as well as stronger shock acceleration, and thus stronger radio and nonthermal X-ray emission. Within this framework, the observed spectral index of the combined PDS spectrum in this work (1.4–2.1) equals that of the radio spectral index of the synchrotron spectra. Indeed, most radio-halo cluster observations typically yield spectra with indexes in this range (e.g., Feretti et al. 2001; Fusco-Femiano et al. 1999), further strengthening the case for IC/CMB. In a forthcoming paper we will examine the connection between the HXR and the radio emission in a sample of clusters in more detail.

The case for IC/CMB is challenged by the clusters A2163, A3266, and A3562 with merger signatures featuring less significant HXR detections from the rest of the merger group. Also, HXR emission for a relaxed cluster A2199 is detected with 2 σ confidence. This implies that the merger is not the only factor responsible for the nonthermal emission in all clusters, which gives room for other models. Even though there is a possibility of Seyfert 2 contribution in the PDS signal (see above), the co-added spectrum is steeper than those observed in AGNs and the indicated extended distribution of HXR emission is also contrary to the central concentration of AGNs in clusters. Thus the current data argue against significant contamination by obscured AGNs in our sample. The nonthermal bremsstrahlung model (e.g., Sarazin & Kempner 2000; Dogiel 2000) predicts spectral slopes of HXR emission consistent with our observations and thus cannot be ruled out by the fit to the current data. However, bremsstrahlung is a very inefficient process (see, e.g., Petrosian 2001; Timokhin et al. 2004), and the huge amount of energy input needed to produce the observed level of hard X-ray emission is ruled out in cases like Coma by X-ray observations (Petrosian 2001).

The secondary electron models usually predict a harder ($\alpha_{\rm ph} \sim 1.5$–1.75) IC/CMB spectrum (Colafrancesco & Blasi 1998; Blasi & Colafrancesco 1999; Miniati et al. 2001) than that indicated by the present observations. If we assume that most of the nonthermal hard X-ray emission originates from the central regions of the clusters, its spectrum is required to be hard ($\alpha_{\rm ph} = 1.3$–1.5; see § 6). In this case, the spatially concentrated hard X-ray emission is consistent with the secondary models, which involve the production of secondary electrons via collisions of relativistic protons that are bound to the cluster gravitational potential wells (Colafrancesco & Blasi 1998). However, this model does not fit well the PDS data at highest energies.

8. CONCLUSIONS

We have studied the hard X-ray emission in the 20–80 keV energy band in a sample of clusters using the *BeppoSAX* PDS instrument. After removing the contributions from the cluster thermal component and from unobscured AGNs, in $\sim$50% of the mildly AGN-contaminated clusters the nonthermal component is detected at 2 σ level, the clusters being A2142, A2199, A2256, A3376, Coma, Ophiuchus, and Virgo. All the clusters detected at 2 σ level exhibit some degree of merger signatures, i.e., deviations from the azimuthally symmetric brightness and temperature distributions (except for A2199). Averaging the PDS 20–80 keV count rates of the relaxed and merger clusters obtains a 2.5 σ detection for the merger group, while the relaxed group count rate is consistent with zero. Assuming a power-law emission model with a photon index of 2.0 at the group average redshifts, the average count rates are consistent with a scenario whereby the relaxed clusters have no HXR component, while mergers do, with a 20–80 keV luminosity of $\sim(10^{43}$–$10^{44})\ h_{50}^{-2}$ ergs s^{-1}.

The co-added spectrum of our sample yields a best-fit photon index of $2.8^{+0.3}_{-0.4}$ for the nonthermal emission in the 12–115 keV band, and we find indication that it has extended distribution. These indications argue against significant

contamination from obscured AGNs, which have harder spectra and a centrally concentrated distribution.

The indicated connection between cluster mergers and the nonthermal hard X-ray emission is consistent with the inverse Compton scattering of the cosmic microwave background photons with merger-accelerated population of relativistic electrons. In this framework, the observed photon index is consistent with a scenario in which a strong acceleration event and consequent strong IC/CMB energy losses take place. In this scenario the measured hard X-ray slope corresponds to a differential momentum spectra of the relativistic electrons with a slope of $\mu = 3.8-5.0$. The consequent synchrotron emission spectrum expected from the same electron population has a spectral index of 1.4–2.1, consistent with radio halo observations of many merger clusters.

The observed slope of the HXR spectrum is also consistent with the predictions of the nonthermal bremsstrahlung model. Even though this fit cannot be ruled out by the current data, the bremsstrahlung model seems to face a strong energetics problem that makes it not a viable physical scenario.

Assuming that most of the nonthermal signal originates in the central regions of clusters, the HXR spectrum is forced to be harder, with a slope $\sim$1.3–1.5, which turns out to be consistent with secondary electron models. However, this model provides a worse fit to PDS data and is thus disfavored by the statistical fit over the primary electron IC/CMB model.

In conclusion, spatially resolved hard X-ray spectroscopy is needed to disentangle the primary and secondary electron models for nonthermal hard X-ray emission in clusters of galaxies.

The *BeppoSAX* satellite is a joint Italian-Dutch program. We thank the staffs of the *BeppoSAX* Science Data and Operations Control Centers for help with these observations. J. N. acknowledges an ESA Research Fellowship and a NASA grant NAG5-9945. We thank T. Clarke, D. Harris, M. Markevitch, M. Page, and H. Tananbaum for useful comments and A. Parmar for his help on the project. M. B. gratefully acknowledges NASA for support.

APPENDIX

THE DETAILS OF THE MODELING OF THE UNOBSCURED AGNS IN INDIVIDUAL CLUSTERS

A85, *A496*, *A2163*, *and A2256*.—There are no cataloged Seyfert 1 galaxies in these clusters or strong point sources in MECS or PSPC in the field.

A1367.—The MECS spectrum of AGN NGC 3862 provides constraints on the reference model, yielding a PDS estimate of $1.0^{+0.4}_{-0.3}\ 10^{-2}$ counts s^{-1}. This value is consistent with HXR emission, and thus the HXR estimate will be very uncertain. The PSPC count rate of NGC 3884 is negligible ($<$1%) of that of NGC 3862 and thus will not change the AGN contribution estimate.

A1795.—There is a Seyfert 1 galaxy, 1E 1346+26.7, 5′ off-axis. Normalizing the reference model to the MECS data gives a PDS estimate of $0.3^{+0.1}_{-0.1}10^{-2}$ counts s^{-1}. In the cluster center there is LINER PKS 1346+26. Its flux estimate cannot be given because of the projection with the bright cluster center. However, LINERS usually have 2–10 keV luminosities 1–3 orders of magnitude smaller than classical Seyfert galaxies (Terashima et al. 2002). AGN RX J1343.9+2712 is outside the PSPC image, and thus an flux estimate cannot be given. The field of A1795, together with Coma, is unusual in its large number of AGNs/QSOs. For A1795 this is probably not a problem though, because HXR emission is negative (consistent with 0) and likely not significantly contaminated by any AGNs. We will use the 1E 1346+26.7 estimate in the following.

A2029.—The MECS data of an AGN, QSO J1511+057, 8′ off-axis, constrain the reference model, yielding a PDS estimate of $0.2^{+0.1}_{-0.1}10^{-2}$ counts s^{-1}. A Seyfert 1, JVAS B1509+054, is located at 29′ off-axis and is thus outside the MECS FOV. It is undetected in the PSPC, and the upper limit of the statistical uncertainties allows 10% of the PDS estimate of QSO J1511+057, which is negligible.

A2142.—A Seyfert 1 galaxy, IC 1166, is outside the PSPC field, and thus the flux estimate cannot be given; 4′ off-axis from the cluster center there is a Seyfert 1 galaxy, 1E 1556+27.4, whose photon index is $\alpha_{\rm ph} = 1.9$ as observed with *ASCA* (Markevitch et al. 1998). The MECS data consistently give $\alpha_{\rm ph} = 1.8 \pm 0.1$. Using this and including the statistical uncertainties of the MECS data, the extrapolated PDS 20–80 keV count rate is $2.2^{+0.7}_{-0.5}10^{-2}$ counts s^{-1}, consistent with the PSPC estimate of 2.9×10^{-2} counts s^{-1}. In A2142 there is another Seyfert 1 galaxy, QSO B1557+272. At 17′ off-axis, the source is quite diffuse in MECS, but the data extracted from a 4′ circle around the source still provide adequate constraints on the normalization of the power-law model. Including statistical uncertainties, the PDS prediction is $0.8^{+0.3}_{-0.2}10^{-2}$ counts s^{-1}. Thus the combined AGN contribution to the PDS 20–80 keV band is $3.0^{+0.8}_{-0.6}10^{-2}$ counts s^{-1}, or 30% of the HXR signal.

A2199.—There are no cataloged Seyfert 1 galaxies in A2199, but X-ray imaging reveals a bright Seyfert 1 galaxy, RXS J16290+4007, of redshift 0.3, located 35′ off-axis and thus outside the MECS FOV. Its PSPC spectrum is not consistent with the reference model. The data can be modeled with a combination of thermal and a power-law model, yielding a temperature of 0.1 keV and a photon index of 2.4 ± 0.1, which makes a negligible contribution to HXR emission. Allowing for spectral hardening toward higher energies, we fitted the PSPC data with our reference model plus MEKAL. The fit is bad, but it yields an estimate for the HXR emission of $0.6^{+0.4}_{-0.3}10^{-2}$ counts s^{-1}, 8% of the HXR emission, thereby decreasing the detection confidence slightly. To be consistent with the treatment of Seyfert 1 galaxies in the rest of the sample, we assume the harder spectrum in the following.

A3266.—A Seyfert 1, J043829.3−614759, at the edge of PSPC gives constraint to the reference model, yielding a PDS estimate of $0.2^{+0.1}_{-0.1}10^{-2}$ counts s^{-1}, 5% of the HXR emission. AGNs C3266−12 and E3266−3 are outside the MECS FOV and undetected in the PSPC. The upper limit allowed by the statistical uncertainties of the PSPC data, fitted with the reference model, yields a PDS estimate below 1% of the level of HXR emission and is thus negligible. In the PSPC there is a bright point source, 1RXS J043356.7−612909, at $04^{\rm h}33^{\rm m}56\overset{\rm s}{.}70$, $-61^\circ 29' 09\overset{''}{.}5$. However, it is not visible in MECS, implying that the source is either very soft or variable, and very faint during *BeppoSAX* observation. Either way it gives no contribution to PDS. Thus we keep the estimate of J043829.3−614759.

A3376.— In the field there is a bright point source 1RX JJ060113.0−401643 at $06^h01^m32^s$, $-40^\circ16'55\farcs7$, 18′ off-axis. There is no information available on its nature. MECS constraints on the spectral slope are poor, but the data constrain well the normalization of the power-law model when we fix the photon index to 1.8 ± 0.2. With this model, we obtain a PDS estimate of $0.3 \pm 0.1 10^{-2}$ counts s^{-1}. A bright source 24′ off-axis coincides with QSO 1WGA J0600.5−3937 and source PKS 0558−396. Using the MECS spectrum, we obtain a PDS estimate of $0.6^{+0.2}_{-0.2}10^{-2}$ counts s^{-1}. A Seyfert 1, J055850.3−403848, in A3376, 50′ off-axis, has a count rate much below the above sources and thus has no effect on the combined estimate of $0.9^{+0.3}_{-0.2}10^{-2}$ counts s^{-1}, ∼10% of the HXR emission.

A3562.—Seyfert 1 1E1335.1−3128 at 60′ off-axis is undetected in PSPC, implying a negligible HXR contribution. A poor cluster SC 1329−313 is included in the PDS FOV.

A3571.—There are no cataloged AGNs or QSOs in the cluster. There is a bright point source, HD 119756, an X-ray binary in the field at (R.A., decl.) = ($13^h45^m41\fs5$, $-33^\circ02'32''$). It is obscured by the MECS calibration source, and the PSPC spectrum indicates a thermal spectrum with $T = 0.4$ keV with no evidence of a power-law component. Thus for A3571 we estimate negligible PDS contribution from point sources.

A3627.—Close to the edge of MECS there is a projected Seyfert 1 galaxy, 1WGA J1611.8−6037. Using the MECS spectrum, we normalized the reference model and obtained a PDS estimate of $6.1^{+2.4}_{-1.5}10^{-2}$ counts s^{-1}. This is consistent with the HXR estimate, which will thus be very uncertain.

A3667.—Seyfert 1 galaxy FRL 339 in A3667 is close to the edge of the MECS FOV. The MECS spectrum constrains the power-law component as $1.9^{+0.2}_{-0.2}$, consistent with the reference model. Using the MECS data, we normalized the reference model and obtained a PDS estimate of $1.0^{+0.4}_{-0.2}10^{-2}$ counts s^{-1}. In the PSPC image there are two other bright noncataloged point sources, 2E 2007.4−5653 at (R.A., decl.) = ($20^h11^m28\fs6$, $-56^\circ44'13''$) and 1RXS J201455.6−565833 at (R.A., decl.) = ($20^h14^m55\fs6$, $-56^\circ58'33''$). The former is undetected in MECS because it is projected at the bright cluster center, and the latter is outside the MECS FOV. Both are classified as X-ray sources. The PSPC data of 2E 2007.4−5653 are consistent with the reference model and gives a PDS estimate of $0.7^{+0.5}_{-0.3}10^{-2}$ counts s^{-1}. The PSPC data of 1RXS J201455.6−565833 are not consistent with the reference model and requires a steeper photon index. The PDS prediction with this model is insignificant. The combined AGN contribution (using FRL 339 and 2E 2007.4−5653) is $1.7^{+0.6}_{-0.4}10^{-2}$ counts s^{-1}, ∼80% of the HXR. The point-source contamination is not discussed in the report on the marginal hard excess of A3667 (Fusco-Femiano et al. 2001).

Coma.—The well-known Seyfert 1 galaxy X-Comae is just at the edge of the MECS FOV. Fusco-Femiano et al. (1999) used MECS data to show that the allowed upper flux level for X-Comae is ∼15% of the hard X-ray excess component at 2–10 keV, using a power-law component with $\alpha_{ph} = 1.8$. We used PSPC data to check the normalization of the reference model. Including the spectral and flux level variation uncertainties, we obtain a PDS 20–80 keV estimate of $0.9^{+0.6}_{-0.6}10^{-2}$ counts s^{-1}, or 10% of the 20–80 keV HXR emission, consistent with Fusco-Femiano et al. (1999). AGN 1E 1258+28.9, at 50′ off-axis, is obscured by the PSPC mirror support structure. The useful data still indicate a count rate similar to that for X-Comae, indicating a significant contribution to PDS. However, the nature of the source is not well known, and the extrapolation toward higher energies is not justified. Seyfert 1 J125710.6+272418 is undetected, and thus its contribution is negligible compared with that of X-Comae. The Coma field contains an unusually high number, 26, of cataloged AGNs/QSOs, perhaps because the Coma field is better studied than others. However, to make up all the HXR emission, seven objects like X-Comae are needed, and this is ruled out for Coma on the basis of the PSPC image.

Cygnus A.—There is a powerful radio galaxy, QSO B1957+405, in the center of Cygnus A. We extracted the central 2′ MECS spectrum and modeled it as a sum of MEKAL and a self-absorbed power law, both absorbed by the galactic N_H. The best-fit photon index $\alpha_{ph} = 1.9^{+0.2}_{-0.2}$ is consistent with the *ASCA* result (Markevitch et al. 1998) and with our reference model. We thus used the 2′ MECS data to normalize the reference power-law model, including a MEKAL model with temperature, metal abundance, and normalization as free parameters. Extrapolating the resulting power-law model to higher energies, we obtained the PDS estimate of $51.1^{+11.8}_{-9.1}10^{-2}$ counts s^{-1}. This is consistent with the total observed PDS emission in this band, and thus the HXR estimate will be uselessly uncertain. We thus reject Cygnus A from further analysis.

Ophiuchus.—There are no cataloged AGNs or QSOs in Ophiuchus. In the PSPC image there is a bright point source, RXS J171209.5−231005, at (R.A., decl.) = ($17^h12^m09^s$, $-23^\circ09'50''$), classified as an X-ray source. It is undetected in MECS because of a projected bright cluster center in the line of sight. The PSPC spectrum exhibits a two-component spectrum consisting of a thermal one with $T \sim 1$ keV and a very steep ($\alpha > 3$) power law, which makes a negligible contribution to the PDS HXR emission.

Perseus.—Perseus hosts a well-known AGN, NGC 1275, in the center. *HEAO I* observations revealed a nonthermal component in the Perseus data at the 20–50 keV band (Primini et al. 1981). The excess was modeled with a power-law model whose best-fit photon index α_{ph} is 1.9 ± 0.3 at 90% confidence. They also report that the source exhibits no significant variations above 25 keV in a timescale of 4 yr. PDS data are of high enough quality to perform a two-component fit if we fix the photon index ($\equiv 1.9$) and MEKAL abundance ($\equiv 0.3$). The resulting temperature, 6.3 ± 0.4 keV, is identical to the *Ginga* value (Allen et al. 1992). The power-law component has a 25–40 keV luminosity of $1.8 \pm 0.5 10^{43}$ ergs s^{-1}, 4 times smaller than The *HEAO I* value, implying variability on a timescale of 20 yr.

Because of the high brightness of cluster thermal emission in the center, compared with that of NGC 1275, the central 2′ MECS data do not provide decent constraints on the internal N_H or the power-law slope of the AGN. However, modeling the central MECS data with MEKAL plus the above power-law component reveals that the power-law model given by the PDS data contributes only a few percent of the total emission. This component modifies the total model only slightly, and the fit is acceptable. If left free, the allowed upper limit for the normalization of the power-law component is 3 times as high as the best value given by PDS data. Thus, the data are consistent with all of the nonthermal emission coming from NGC 1275. We thus reject Perseus from further analysis.

Virgo.—Virgo has an active nucleus, M87, and a jet in the center. *XMM-Newton* data yield power-law slopes of 2.2 ± 0.2 and 2.5 ± 0.4 for the nucleus and the bright knot in the jet (Böhringer et al. 2001) at 90% confidence, and no indication of excess

absorption. The 2′ MECS data do not provide good constraint on the slope of the nonthermal component. We thus fit the 2′ MECS data with a model consisting of MEKAL and a power law, both absorbed by the galactic $N_{\rm H}$, fixing the photon index to 2.3, based on the *XMM-Newton* observations (Böhringer et al. 2001), thus obtaining the normalization and its uncertainty for the power-law component. We determined the thermal component of Virgo by using the above-determined central power-law model together with MEKAL when fitting the 0–8′ keV MECS data. The best-fit parameters $T = 2.35 \pm 0.04$ keV and abundance 0.49 ± 0.04 solar are consistent with *XMM-Newton* results. Letting only the thermal model normalization be a free parameter, we then normalized this model to the PDS FOV using 12–20 keV PDS data. According to this model, M87 contributes 17% ± 3% of the nonthermal emission in the 20–80 keV band. Allowing spectral variability for M87, we repeated the above exercise keeping $\alpha_{\rm ph}$ at 2.0 and 1.7. The resulting M87 contribution to the HXR emission is 20%–30% and 30%–50%, respectively. Unless the spectrum of M87 has a strong hard excess, the nonthermal PDS signal of Virgo cannot be explained entirely by M87. We keep the $\alpha_{\rm ph} = 2.3$ results, i.e., an M87 contribution of $4.5 \pm 0.7^{10^{-2}}$ counts s^{-1} and the thermal model prediction of $0.3 \pm 0.2^{10^{-2}}$ counts s^{-1} to the PDS 20–80 keV band.

REFERENCES

Allen, S. W., et al. 1992, MNRAS, 254, 51
Arnaud, J., et al. 2001, A&A, 365, L67
Bell, A. R. 1978a, MNRAS, 182, 147
———. 1978b, MNRAS, 182, 443
Blasi, P., & Colafrancesco, S. 1999, Astropart. Phys., 12, 169
Böhringer, H., et al. 1994, Nature, 386, 828
———. 1996, ApJ, 467, 168
———. 1998, A&A, 334, 789
———. 2001, A&A, 365, L181
Cappi, M., et al. 2001, ApJ, 548, 624
Colafrancesco, S. 1999, in Diffuse Thermal and Relativistic Plasma in Galaxy Clusters, ed. H. Boehringer et al. (MPE Rep. 271; Garching: MPE), 295
Colafrancesco, S., & Blasi, P. 1998, Astropart. Phys., 9, 227
Colafrancesco, S., & Mele, B. 2001, ApJ, 562, 24
Comastri, A., et al. 1995, A&A, 296, 1
de Grandi, S., & Molendi, S. 1999a, A&A, 351, L45
———. 2002, ApJ, 567, 163
Della Ceca, R., et al. 2000, A&A, 353, 498
Dickey, J., & Lockman, F. 1990, ARA&A, 28, 215
Dogiel, V. 2000, A&A, 357, 66
Ebeling, H., Voges, W., Bohringer, H., Edge, A. C., Huchra, J. P., & Briel, U. G. 1996, MNRAS, 281, 799
Ensslin, T., Lieu, R., & Biermann, P. 1999, A&A, 344, 409
Ettori, S., Allen, S., & Fabian, A. 2001, MNRAS, 322, 187
Ettori, S., et al. 2000, MNRAS, 318, 239
Feretti, L. 2003, in ASP Conf. Ser. 301, Matter and Energy in Clusters of Galaxies, ed. S. Bowyer & C.-Y. Hwang (San Francisco: ASP)
Feretti, L., Fusco-Femiano, R., Giovannini, G., & Govoni, F. 2001, A&A, 373, 106
Frontera, F., et al. 1997a, A&AS, 122, 357
———. 1997b, Proc. SPIE, 3114, 206
Fujita Y., & Sarazin, C. 2001, ApJ, 563, 660
Fukazawa, Y., et al. 2001, ApJ, 546, L87
Fusco-Femiano, R., et al. 1999, ApJ, 513, L21
———. 2000, ApJ, 534, L7
———. 2001, ApJ, 552, L97
———. 2003, A&A, 398, 441
Gilli, R., Risaliti, G., & Salvati, M. 1999, A&A, 347, 424
Giovannini, G., Tordi, M., & Feretti, L. 1999, NewA, 4, 141
Grupe, D., et al. 2001, A&A, 367, 470
Hasinger, G., et al. 2001, A&A, 365, L45
Hughes, J., Butcher, J., & Stewart, G. 1993, ApJ, 404, 611
Kaastra, J. S., et al. 1999, ApJ, 519, L119
Maiolino, R., & Rieke, G. H. 1995, ApJ, 454, 95
Markevitch, M.,, et al. 1996, ApJ, 456, 437
———. 1998, ApJ, 503, 77
———. 1999a, ApJ, 521, 526
———. 1999b, ApJ, 527, 545
Markowitz, A., & Edelson, R. 2001, ApJ, 547, 684
Martini, P., et al. 2002, ApJ, 576, L109
Matsuzawa, H., Matsuoka, M., Ikebe, Y., Mihara, T., & Yamashita, K. 1996, PASJ, 48, 565
Miniati, F., et al. 2001, ApJ, 562, 233
Mohr, R. 1999, ApJ, 517, 627
Molendi, S., DeGrandi, S., & Fusco-Femiano, R. 2000, ApJ, 534, L43
Molnar, M. R., et al. 2002, ApJ, 573, L91
Page, M. J. 1998, MNRAS, 298, 537
Perola, G. C., et al. 2002, A&A, 389, 802
Petrosian, V. 2001, ApJ, 557, 560
Primini, F. A., et al. 1981, ApJ, 243, L13
Randall, S., Sarazin, C., & Ricker, P. 2002, ApJ, 577, 579
Risaliti, G., Maiolino, R., & Salvati, M. 1999, ApJ, 522, 157
Sarazin, C. 1999, ApJ, 520, 529
Sarazin, C., & Kempner, J. C. 2000, ApJ, 533, 73
Sarazin, C. L., et al. 1998, ApJ, 498, 606
Schindler, S., et al. 1997, A&A, 317, 646
Shibata, R., et al. 2001, ApJ, 549, 228
Sun, H., & Murray, S. S. 2002, ApJ, 577, 139
Takizawa, M., & Naito, T. 2000, ApJ, 535, 586
Terashima, Y., et al. 2002, ApJS, 139, 1
Timokhin, A. N., Aharonian, F. A., & Neronov, A. Yu. 2004, A&A, in press (astro-ph/0305149)
Valinia, A., et al. 1999, ApJ, 525, 47
Watanabe, M., et al. 2001, PASJ, 53, 605
White, R. E., et al. 1994, ApJ, 433, 583